Opto-Electronic Advances

CN 51-1781/TN ISSN (Print) 2096-4579 ISSN (Online) 2097-3993

Scalable photonic crystal scintillators for high-performance X-ray imaging in photon-starved regimes

Yao Zhu, Chentao Li, Sijun Cao, Junan Lai, Peng He, Qiang Wang, Xiong Xiao, Kaifeng Liu*, Yuchong Ding* and Peng Feng*

Citation: Zhu Y, Li CT, Cao SJ et al. Scalable photonic crystal scintillators for high-performance X-ray imaging in photon-starved regimes. *Opto-Electron Adv* **10**, 260038 (2027).

https://doi.org/10.29026/oea.2027.260038

Received: 25 February 2026; Accepted: 27 July 2026; Published online: 17 September 2026

OEA | Opto-Electronic Advances

Article

2027, Vol. , No.

Open Access

Scalable photonic crystal scintillators for high-performance X-ray imaging in photon-starved regimes

Yao Zhu[1,2], Chentao Li[3], Sijun Cao[4], Junan Lai[5], Peng He[1,6], Qiang Wang[2,5], Xiong Xiao[2], Kaifeng Liu[7]*, Yuchong Ding[2]* and Peng Feng[1,6]*

Abstract: High-density inorganic scintillators play a pivotal role in X-ray imaging owing to their strong stopping power and efficient emission in the visible regime. However, their practical performance is fundamentally constrained by refractive-index mismatch, which traps a large fraction of generated photons through total internal reflection. Although photonic crystal structures offer a promising route for enhancing light extraction, scalable large-area integration onto scintillator substrates remains a significant challenge. Here, we propose a scalable self-assembly-based fabrication strategy for large-area photonic crystal scintillators, enabling the formation of a 25-mm-scale continuous PS-nanosphere PhC monolayer with locally verified HCP packing on the scintillator surface. The resulting photonic crystal facilitates momentum compensation via Bragg diffraction, thereby coupling confined guided wave modes to free-space radiation. Under X-ray excitation, this diffraction-mediated extraction mechanism experimentally yields a 4.64-fold enhancement in light output and a 13 dB improvement in signal-to-noise ratio for radiographic imaging. The measurable gain in detection sensitivity suggests this scalable fabrication strategy is a promising approach for high-performance X-ray detection in photon-starved applications, including low-dose medical diagnostics and security screening.

Keywords: scintillator; photonic crystals; self-assembly; X-ray imaging; light extraction

DOI: 10.29026/oea.2027.260038 | CSTR: 32247.14.oea.2027.260038

Citation: Zhu Y, Li CT, Cao SJ et al. Scalable photonic crystal scintillators for high-performance X-ray imaging in photon-starved regimes. *Opto-Electron Adv*, 260038 (2027).

1 Introduction

Scintillation is the emission of visible light from materials in response to high-energy radiation, underpinning a wide range of radiation detection and imaging technologies[1]. It is particularly prominent in X-ray imaging and characterization, where scintillators function as the key components converting X-ray photons into detectable scintillation photons. As a result, these materials are extensively used in medical diagnostic equipment such as digital radiography, positron emission tomography (PET), single photon emission computed tomography (SPECT) scanners and X-ray computed tomography (CT), among others[2–6]. Recent advances in transparent luminescent nano-glass-ceramics, luminescent metal-organic framework glasses, near-infrared-emitting lead-free perovskite scintillators, and TADF-enabled hafnium chloride array scintillator screens have further expanded the material and design space for X-ray imaging[7–10]. Among the various material classes, high-density inorganic scintillators are widely utilized in low-dose medical diagnostics and security screening applications due to their exceptional X-ray attenuation, high light yield and fast decay times[11,12]. However, despite these intrinsic merits,

Received: 25 February 2026

Accepted: 27 July 2026

Published online: 17 September 2026

[1]The Key Laboratory of Optoelectronic Technology & Systems (Ministry of Education), College of Optoelectronic Engineering, Chongqing University, Chongqing 400044, China; [2]Research & Development Center of Material and Equipment, China Electronics Technology Group Corporation No. 26 Research Institute, Chongqing 400060, China; [3]Fu Foundation School of Engineering and Applied Science, Columbia University, New York NY 10027, USA; [4]Department of Electronic Engineering, Chinese University of Hong Kong, Hong Kong SAR 999077, China; [5]Department of Radiology, Xinqiao Hospital, Army Medical University, Chongqing 400037, China; [6]ICT NDT Engineering Research Center (Ministry of Education), Chongqing University, Chongqing 400044, China; [7]Department of Physics, Stevens Institute of Technology, Hoboken NJ 07030, USA.

*Correspondence: KF Liu, E-mail: kliu31@stevens.edu; YC Ding, E-mail: dingyc@cetccq.com.cn; P Feng, E-mail: coe-fp@cqu.edu.cn

their practical performance is fundamentally constrained by severe refractive index mismatch between the scintillator and its surrounding medium[13]. This mismatch results in severe photon trapping via total internal reflection (TIR), confining up to ~90% of the generated photons within waveguide modes rather than escaping the scintillator[14]. The inefficiency is further exacerbated in high-resolution applications, which necessitate ultrathin scintillators to suppress lateral light scattering. However, such reduced thickness inherently compromises X-ray stopping power, resulting in scarce luminescence output, especially under low-dose irradiation. This cumulative signal loss significantly degrades detection sensitivity and signal-to-noise ratio (SNR), constituting a long-standing bottleneck for high-performance imaging systems[15,16]. Complementary to detector-side optimization, interpretable computational approaches, such as multi-Gaussian cluster variance reduction, have also been developed to enhance low-dose CT image quality[17].

To overcome this optical confinement at the detector level, photonic crystals (PhCs) have been employed to pattern the scintillator surface at the emission-wavelength scale, enabling the diffraction-mediated extraction of otherwise confined modes[18–20]. While the enhancement of light extraction efficiency (LEE) via PhCs has been theoretically established[21–23], the practical implementation of such devices remains hindered by challenges in scalable manufacturing. Currently, top-down fabrication approaches, such as electron beam or X-ray lithography, offer deterministic control over light coupling structures. Nevertheless, these methods generally require sophisticated lithographic infrastructure and multi-step processing, which may limit their practical implementation over large scintillator areas[24–26]. Furthermore, despite providing nanoscale resolution and repeatability, these techniques are generally incompatible with chemically sensitive or mechanically fragile substrates, including bulk scintillator crystals[23,27]. On the other hand, bottom-up approaches —such as self-assembly, nanoimprinting and chemical vapor deposition (CVD) —have been explored as solution-processable or lithography-free alternatives to conventional photolithography[28–32]. Yet, adapting these methods for scintillator substrates has historically been impeded by poor long-range order. Most commonly used self-assembly techniques (e.g., dip coating and vertical deposition) typically yield polycrystalline domains, random cracks, and localized vacancies at the macroscale[33,34]. These defects act as parasitic scattering centers severely constraining the achievable LEE while inducing spatial inhomogeneities and imaging artifacts that degrade high-performance systems[35–37]. For maximizing the technological potential of self-assembled PhCs, fabrication strategies are required to reconcile the cost-effectiveness of bottom-up approaches with the high LEE and high-quality structural precision and uniformity through top-down methods.

Here, we demonstrate a scalable strategy for fabricating large-area PhC scintillators. By leveraging Marangoni-driven[38,39] self-assembly of polystyrene (PS) nanospheres, we realize a continuous hexagonal close-packed (HCP) PhC monolayer covering the surface of a 25-mm-diameter cerium-doped gadolinium aluminum gallium garnet (GAGG:Ce) wafer—a substrate selected for its superior light yield and X-ray stopping power relative to conventional garnets[40–42]. Numerical simulations and angle-resolved spectroscopy confirm that this ordered monolayer functions as an efficient diffraction grating, bridging the momentum mismatch to couple large-angle guided modes into free-space radiation via Bragg diffraction[23,43,44]. Experimentally, the integrated PhC scintillator exhibits a 4.64-fold enhancement in light extraction and, critically, a 13 dB improvement in SNR compared with that of the reference scintillator. Although this diffraction-mediated extraction entails a modest trade-off in spatial resolution (approximately 17%), it provides a decisive advantage by substantially enhancing detection performance in low-dose regimes, where photon scarcity constitutes the dominant limiting factor. By combining enhanced imaging performance with a scalable fabrication process, this work provides a practical pathway toward large-area PhC scintillators and high-sensitivity X-ray detector platforms.

2 Structural design and numerical simulations

Addressing the extraction bottleneck induced by the high refractive index of GAGG:Ce ($n_{Sc} \approx 1.9$), we designed a surface-integrated PhC architecture capable of managing photon momentum at the scintillator-air interface (shown in Fig. 1). The device features a large-area monolayer of PS nanospheres ($n_{PhC} \approx 1.59$) self-assembled directly onto the

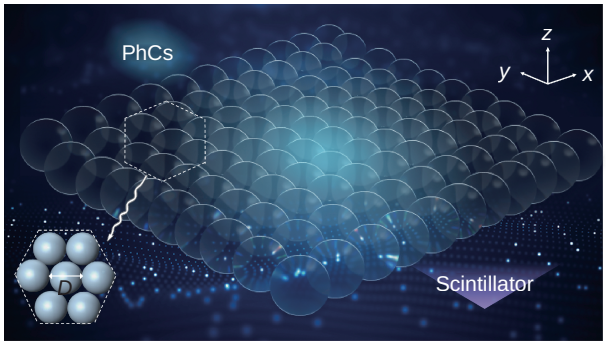

Fig. 1 | Schematic illustration of the self-assembled photonic crystal (PhC) scintillator. The device comprises a monolayer of polystyrene (PS) nanospheres self-assembled on a high-refractive-index GAGG:Ce scintillator. The central bright spot within the substrate indicates the scintillation process, where absorbed X-ray energy is converted into visible light emission. The unit cell composed of a hexagonal close-packed (HCP) lattice with a diameter (D = 500 nm), inserted in the lower left corner, is periodically arranged along x- and y-directions to form a large diffraction grating.

scintillator substrate. As depicted in the inset of Fig. 1, the nanospheres self-organize into a highly ordered HCP lattice with a uniform diameter of $D = 500$ nm. This specific geometric periodicity is engineered to act as a diffraction grating, modulating the effective refractive index profile to change the waveguide boundary conditions. By introducing this periodic dielectric contrast, the structure is designed to couple the otherwise confined high-angle guided modes into leaky modes compatible with free-space radiation.

The diffraction-mediated extraction mechanism and the resulting electromagnetic field profile were simulated using three-dimensional finite-difference time-domain (FDTD) simulations, and Section 1.6 in the Supplementary information details the specific implementation of the FDTD method. The periodic dielectric structure is introduced to function as a diffraction grating, which provides the necessary momentum compensation to overcome TIR. When the in-plane wavevector component $\boldsymbol{k}_{\parallel}$ satisfies $|\boldsymbol{k}_{\parallel}| > k_0 n_{\mathrm{air}}$, where $k_0 = 2\pi/\lambda$, optical energy is confined within the substrate. However, introducing the reciprocal lattice vector $\boldsymbol{G}_{m,n}$ overcomes this confinement by compensating for the momentum mismatch between the confined guided modes and the free-space light cone. This extraction mechanism is governed by the Bragg momentum conservation condition: $\boldsymbol{k}_{\parallel,\mathrm{out}} = \boldsymbol{k}_{\parallel,\mathrm{in}} + \boldsymbol{G}_{m,n}$[14]. Consequently, confined guided modes with large in-plane momentum are coupled into the nanosphere array and folded back into the light cone ($|\boldsymbol{k}_{\parallel,\mathrm{out}}| < k_0$)[45]. Through this diffraction-mediated momentum coupling, optical energy is efficiently transferred from guided states to free space.

The direct consequence of this momentum coupling is visualized in the steady-state electric field intensity distributions (Fig. 2(a)). In the planar reference (left), optical energy is strictly confined within the high-index medium, exhibiting a characteristic evanescent decay ($E(z) \propto \mathrm{e}^{-\kappa z}$) on the air side. In stark contrast, the PhC-integrated interface (right) facilitates a radiative leakage channel. Here, the near-field interactions with the periodic lattice effectively couple the otherwise confined modes into propagating free-space radiation.

This diffraction-mediated extraction effect is further corroborated by the angle-resolved optical transmission spectra (Fig. 2(b)). Distinct from the sharp transmission cutoff at the critical angle ($\theta_c \approx 33°$) observed in the reference interface, the PhC-integrated system displays rich, high-intensity dispersion branches extending deep into the theoretical "forbidden region" ($\theta > \theta_c$). These dispersive features correspond to the diffraction signatures of Bloch modes coupled out by the lattice[46]. Cross-sectional transmission profiles (Fig. S1) further clarify this phenomenon: The spectral features in the $\theta > \theta_c$ region appear as sharp, wavelength-dependent resonance peaks rather than the incoherent background typical of random scattering. These discrete transmission bands confirm that the extraction mechanism is driven by coherent Bragg diffraction, ensuring efficient and selective outcoupling of trapped photons over a broad angular bandwidth. Generally, these simulation results demonstrate that the self-assembled PhC layer functions distinctively as a diffractive grating rather than a geometric scatterer, effectively compensating for the momentum mismatch between the high-refractive-index scintillator and the surrounding medium, thereby enhancing the LEE.

3 Results and discussion

For implementing the proposed diffraction-mediated extraction mechanism, we developed a modified interfacial self-assembly strategy driven by the Marangoni effect (Fig. 3(a)). Compared with conventional dip-coating techniques, which are prone to multilayer stacking and localized defects, our approach utilizes the rapid spreading of ethanol-dispersed PS nanospheres ($D = 500$ nm) at the air-water interface. An optimized ethanol-to-water binary solvent ratio of 1:1 (V/V) induces a steep surface-tension gradient, driving uniform lateral transport and facilitating the formation of a macroscopic, high-quality monolayer prior to disordered aggregation.

Following the initial spreading, the introduction of a surfactant (sodium dodecyl sulfate, SDS) induces strong lateral capillary forces, compacting the initially loose domains into a densely packed monolayer. This capillary-force-assisted compaction promotes local rearrangement of PS nanospheres and helps reduce small vacancies and discontinuities within the monolayer. To facilitate the robust transfer of this fragile monolayer, the GAGG:Ce substrate was pre-treated with oxygen plasma prior to deposition to enhance interfacial wettability (contact angle < 5°). The subsequent transfer process was executed via a vibration-free drainage technique, where the subphase descent rate was precisely controlled (< 0.25 mm/s), effectively suppressing contact line pinning effects and crack formation.

Distinct from the planar reference (Fig. 3(b)), the PhC-integrated scintillator displays pronounced iridescence over the 25-mm-diameter surface under white-light illumination, indicating the formation of a continuous surface PhC coating with angle-dependent diffraction behavior. We note that the hue and brightness are not perfectly uniform across the photograph. Such spatial variations are consistent with the angle-dependent grating diffraction of self-assembled colloidal crystals, for which the apparent structural color depends on the illumination/observation geometry and the in-plane orientation of local crystalline domains[44,47]. Therefore, Fig. 3(c) is used here as qualitative evidence of large-area iridescent coverage rather than as quantitative proof of perfectly uniform thickness or coloration. This macroscopic structural coloration suggests continuous PhC coverage and angle-dependent diffraction, which functions as an efficient diffraction grating capable of selectively redistributing the visible spectrum. Complementary microscopic characteriza-

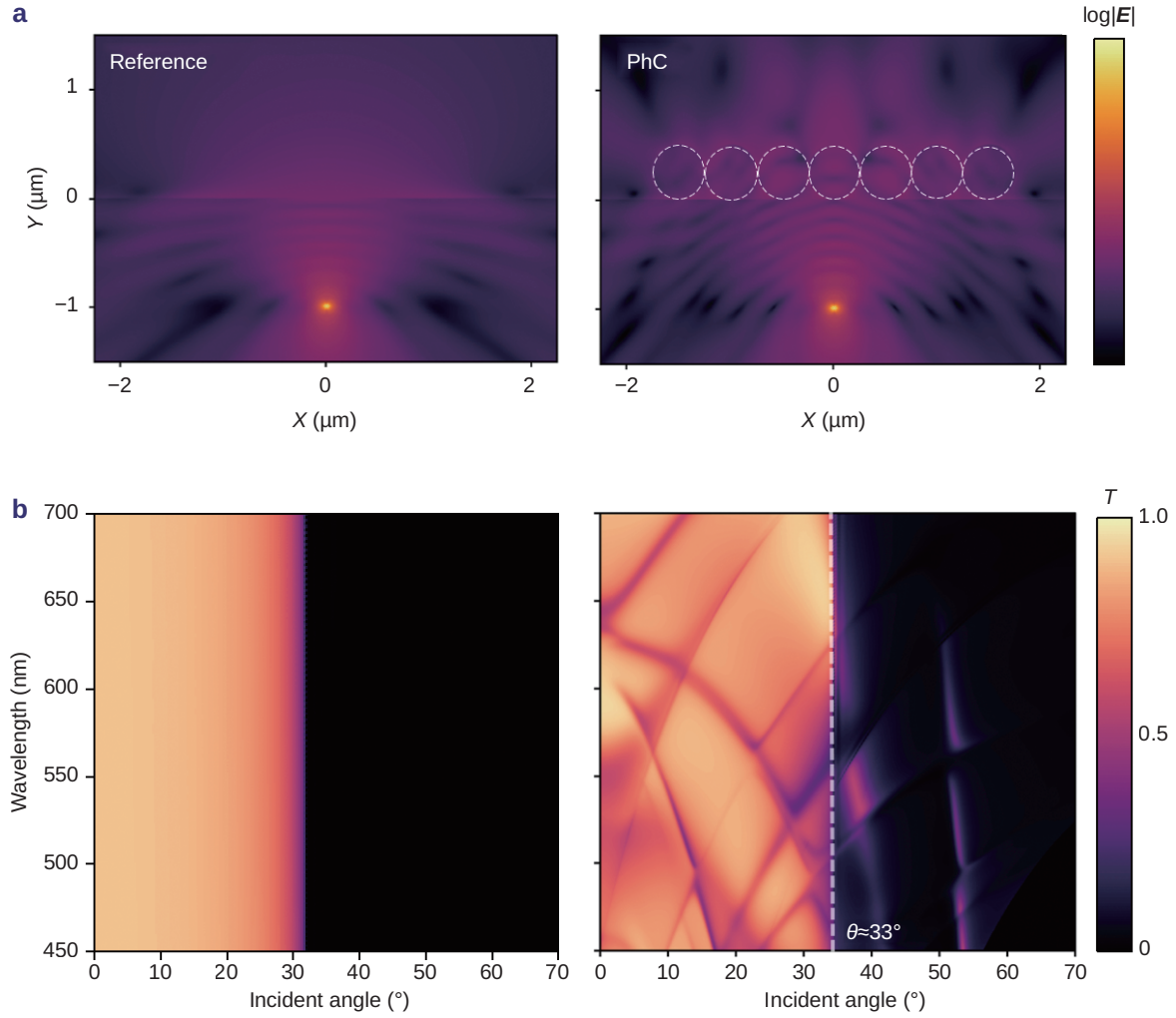

Fig. 2 | Numerical verification of the diffraction-mediated extraction mechanism. (a) Cross-sectional distributions of the electric field magnitude (log|***E***|) calculated by FDTD simulations at λ=550 nm, presented in the left (reference) and right (PhC). (b) Angle-resolved optical transmission spectra for the reference (left) and PhC (right) models.

tion by scanning electron microscopy (SEM) further confirms the high fidelity of the self-assembled structure. To further quantify the local packing quality, we performed coordinate-based SEM analysis at five representative positions of the 25-mm sample, including the center, two middle-radius regions, and two edge regions (Table S10). The extracted particle-center statistics show relatively stable nearest-neighbor spacing and locally verified HCP packing within the sampled intact regions. As shown in Fig. 3(d), the monolayer maintains high continuity throughout the fields of view. High-magnification images (Fig. 3(e)) reveal a well-ordered HCP lattice arrangement of the nanospheres.

We systematically characterized the emission properties of the PhC-integrated scintillator under diverse excitation conditions (Fig. 4(a), experimental setup and spectral acquisition details in Supplementary information Section 1). The spectra are plotted as relative intensities, $I/I_{\mathrm{ref,max}}$, where $I_{\mathrm{ref,max}}$ is the peak intensity of the condition-matched planar reference spectrum measured under the same excitation source and collection angle. The planar reference sample denotes the bare GAGG:Ce scintillator without the PS-nanosphere PhC layer, and θ is defined as the collection angle with respect to the surface normal of the scintillator. Under X-ray excitation, the PhC-integrated scintillator exhibits a 4.64-fold increase in integrated emission intensity over 450–700 nm and a 5.0-fold increase in peak intensity at approximately 550 nm under normal collection (Fig. 4(a), X-ray, θ = 0°). Crucially, this enhancement remains highly robust against angular variations: even at an oblique detection angle (Fig. 4(a), X-ray, $\theta = 45°$), the device retains a 3.46-fold increase in integrated intensity and a 4.0-fold enhancement at the emission peak. To further decouple the depth-dependent extraction dynamics, we compared excitation conditions characterized by distinct penetration depths. Under ultraviolet (UV) excitation (Fig. 4(a), UV, $\theta = 45°$), photon generation is strictly confined to the near-surface

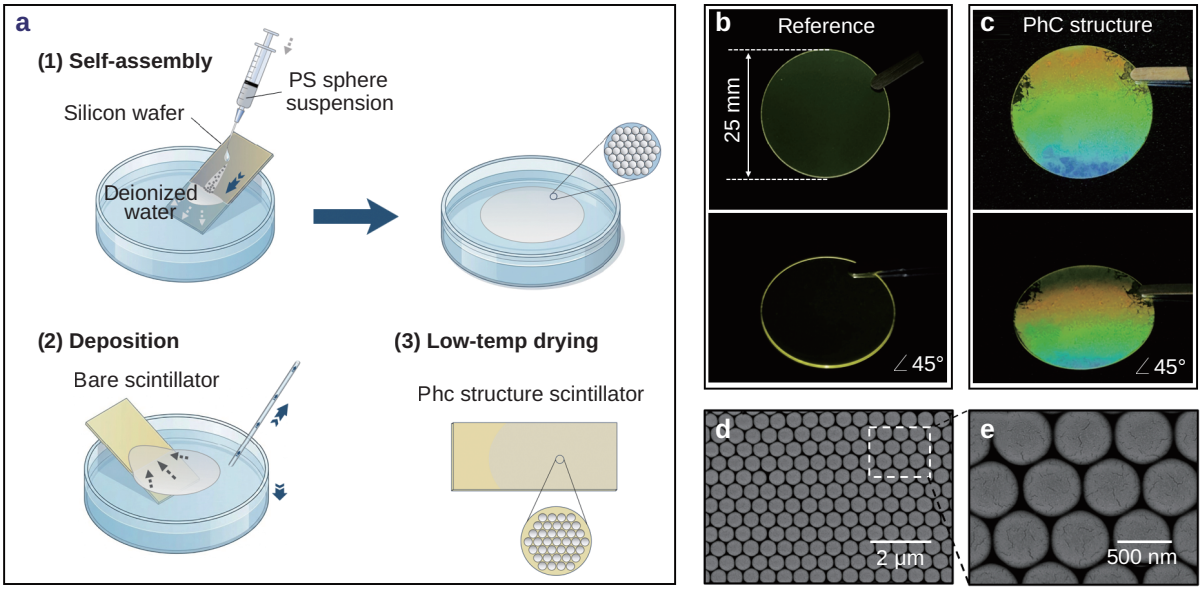

Fig. 3 | Scalable fabrication of PhC-enhanced scintillators via self-assembly. (a) Schematic illustration of the fabrication workflow: (1) Self-assembly: A HCP monolayer of PS nanospheres is assembled at the air-water interface via the ethanol-mediated Marangoni effect. (2) Deposition: The floating monolayer is conformally transferred onto the scintillator substrate via a controlled water drainage process. (3) Drying: The sample is dried at 45 °C to remove residual solvent and enhance adhesion. (b–c) Macroscopic photographs of (b) the bare reference and (c) the PhC-integrated scintillator under white light illumination. (d–e) Top-view SEM images of the PhC array. The magnified image is shown in (e).

region of the scintillator. While this surface excitation mode yields a substantial ~3-fold peak output enhancement, it is notably inferior to the ~4.0-fold enhancement observed under the deeper-penetrating X-ray excitation regime at identical detection angles (Fig. 4(a) with X-ray $\theta = 45°$ and UV $\theta = 45°$). This observation indicates that the PhC functions not merely by modulating surface states, but serves as a global diffraction grating that effectively extracts guided modes from the entire scintillator volume, independent of the photon generation depth.

It should be noted that the measured 4.64-fold enhancement does not represent a complete light-extraction limit, but rather the collected intensity enhancement under the present optical configuration. As a simplified physical reference, the critical angle of the GAGG:Ce/air interface is estimated to be approximately 31.8° by taking $n_{GAGG}\approx1.9$ near the emission maximum. Under an isotropic-emission approximation, only about 15% of the upward emission lies within the direct escape cone of a planar interface, corresponding to an idealized enhancement scale of approximately 6–7 if the otherwise trapped modes could be fully redirected into extractable directions. The observed enhancement is therefore below this simplified limit, which can be attributed to finite spectral and angular diffraction bandwidths, Fresnel reflection at the GAGG/PS/air interfaces, angular redistribution beyond the collection acceptance, imperfect filling fraction, and defect-induced incoherent scattering from vacancies, domain boundaries, and local cracks.

To identify the physical mechanism of the enhancement, and in particular to distinguish improved light extraction from a possible modification of the radiative decay rate induced by the Purcell effect[18], we performed time-resolved photoluminescence (TR-PL) measurements on the reference and PhC-integrated samples (Fig. 4(c)). The decay profiles were fitted using a bi-exponential function, $I(t) = I_0 + A_1\exp(-t/\tau_1) + A_2\exp(-t/\tau_2)$, with the fitting parameters summarized in Table S6. The reference and PhC-integrated samples show comparable average lifetimes of 56.81 ns and 55.38 ns, respectively, indicating that the PhC layer does not induce a pronounced modification of the intrinsic scintillation decay dynamics or a strong Purcell effect. Therefore, the observed emission enhancement is mainly attributed to PhC-assisted diffractive light extraction of waveguided modes otherwise confined by total internal reflection. Meanwhile, incoherent scattering arising from inevitable structural imperfections in the self-assembled PhC layer may also contribute to the broadband outcoupling enhancement. Complementing this analysis, the nearly identical photoluminescence excitation (PLE) spectra (Fig. 4(d)) further confirm that our fabrication process preserves the intrinsic electronic structure of the GAGG:Ce material. Additionally, angle-resolved spectroscopy (Fig. 4(e)) reveals the diffraction-driven mechanism of the extraction enhancement. Differing from the isotropic Lambertian emission profile of the reference sample, the PhC sample exhibits a

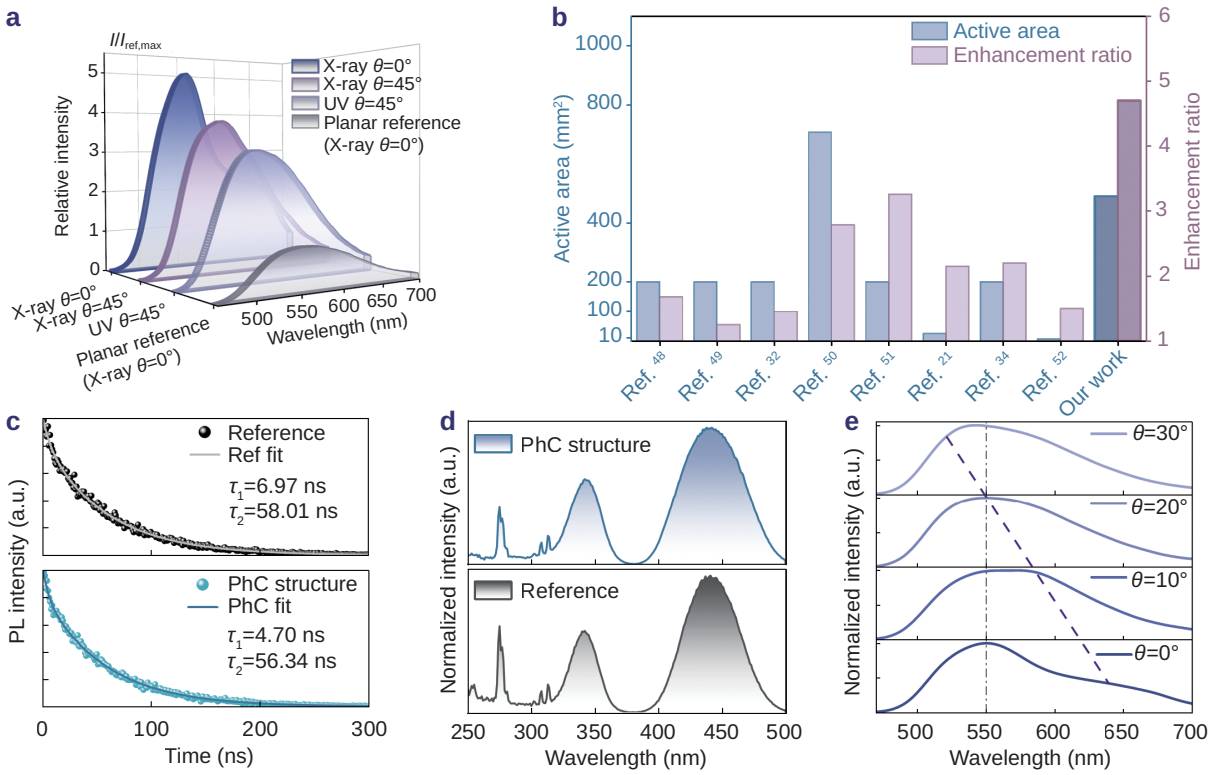

Fig. 4 | Spectroscopic characterization and mechanism verification. (a) Relative emission spectra of the PhC-integrated and planar reference GAGG:Ce samples under X-ray and UV excitation at different collection angles (θ). The planar reference sample denotes the bare GAGG:Ce scintillator without the PS-nanosphere PhC layer. (b) Benchmarking of active device area versus light output enhancement ratio. Representative self-assembled PhC scintillators reported in the literature are included for comparison (refs. [21,32,34,48–52]). Detailed parameters are provided in Table S1. (c) Time-resolved photoluminescence (TR-PL) decay profiles. (d) PLE spectra of the PhC-integrated and reference samples. (e) Angle-resolved emission spectra of the PhC sample (offset for clarity). The dashed line traces the spectral blue-shift of the diffraction resonance peak with increasing detection angle (θ).

distinct dispersive spectral evolution. As the detection angle θ increases from 0° to 30°, the diffraction resonance peak undergoes a pronounced blue shift. This dispersion behavior aligns precisely with the momentum matching condition of a diffraction-based out-coupling grating, where the parallel wavevector component satisfies the Bragg condition: $\boldsymbol{k}_{\parallel} = \boldsymbol{k}_{\text{guided}} \pm m\boldsymbol{G}$. The correlation between the experimental peak shift and the theoretical dispersion relation supports that the hexagonal lattice provides the necessary reciprocal-lattice momentum to compensate for the mismatch between guided modes and free-space radiation, effectively converting high-angle guided modes into free-space radiation.

With the high-efficiency extraction mechanism validated, Fig. 4(b) benchmarks our device against representative self-assembled PhC scintillators (detailed parameters are provided in Table S1), focusing on two critical indicators (enhancement ratio and active area[14]) in practical applications. In general, the active area determines the imaging field of view and the enhancement ratio is affected by the structural order of the PhC monolayer. Existing self-assembled devices typically exhibit modest enhancement factors (averaging ~2.0), constrained by the inherent structural disorder of conventional assembly[32–34,51,52]. Such defects act as scattering centers that degrade spatial resolution, restricting prior studies primarily to non-imaging energy detection[21,48–50]. In contrast, enabled by continuous PhC coverage and locally ordered HCP domains, this work realizes a macroscopically active imaging area of ~490 mm² (Φ = 25 mm). Within this active area, the integrated light-output enhancement averaged 4.63 ± 0.13 for the central regions of three independently fabricated samples. Considering one additional edge measurement from Sample 1, the average enhancement over four measured positions was 4.64 ± 0.11 (Fig. S7). For comparison, representative lithography-based PhC scintillators, including electron-beam lithography (EBL) and X-ray interference lithography (XIL) approaches, are summarized in Table S2. The comparison suggests that the present self-assembled structure can achieve comparable light-output enhancement while enabling large-area integration.

We evaluated how the integration of the PhC monolayer affects the actual X-ray imaging quality, with particular emphasis on balancing the trade-off between SNR and spatial resolution. Using the high-resolution imaging system illustrated in Fig. 5(a) (optical configuration details in

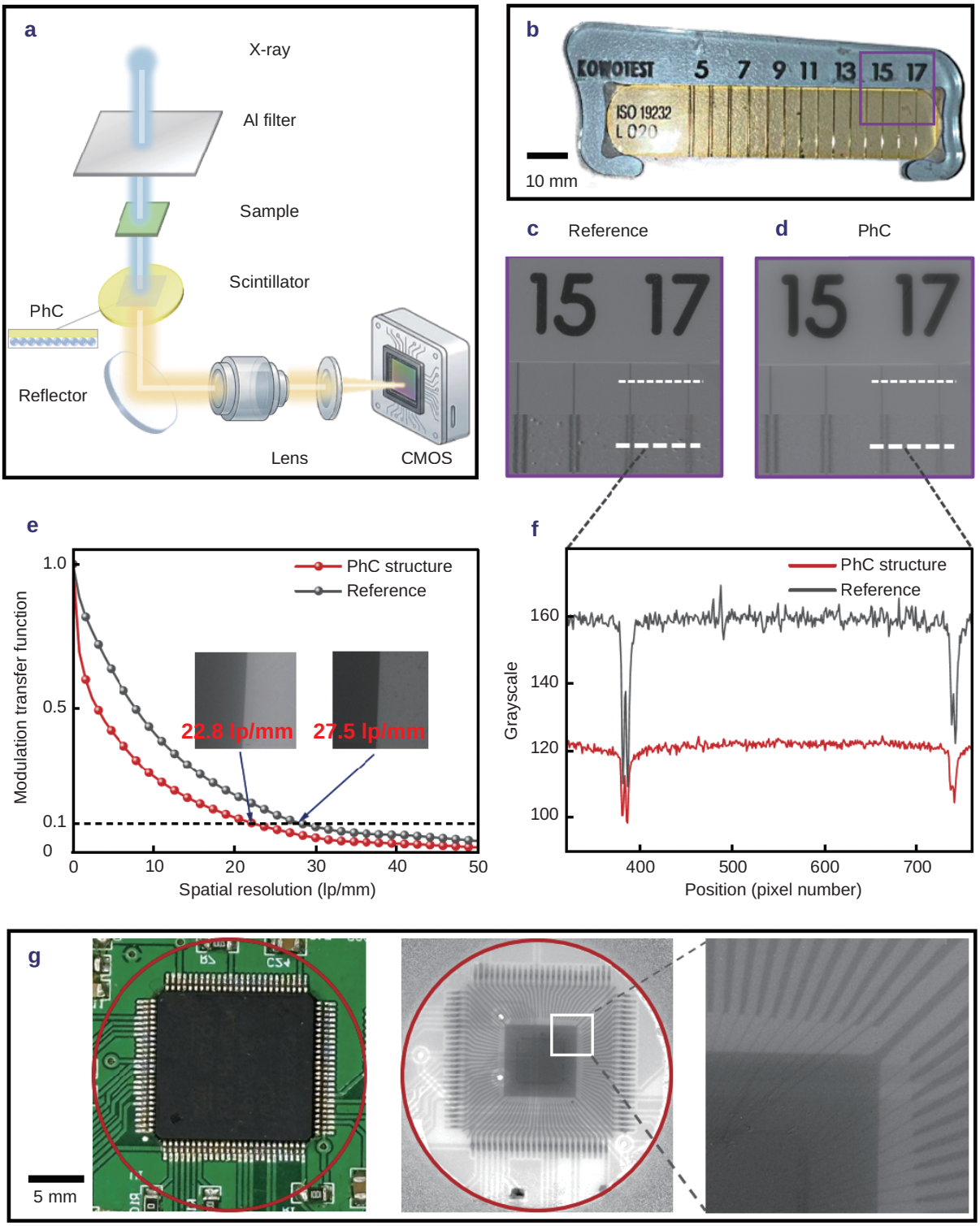

Fig. 5 | X-ray imaging performance characterization. (a) Schematic illustration of the high-resolution X-ray imaging optical experimental setup. (b) Photograph of the standard duplex-wire type image quality indicator (ISO 19232 series). (c–d) X-ray radiographs of the line-pair region acquired using (c) the reference and (d) the PhC-enhanced scintillator. (e) MTF curves calculated from slanted-edge measurements. The limiting spatial resolution, defined at MTF = 0.1, decreases moderately from 27.5 lp/mm for the reference sample to 22.8 lp/mm for the PhC-integrated sample. (f) Grayscale intensity cross-sections extracted across the line pairs in (c) and (d). (g) Demonstration of practical applicability via X-ray imaging of a packaged IC chip.

Supplementary information Section 1), X-ray imaging was performed on a standard duplex-wire type image quality indicator (IQI) according to ISO 19232, as shown in Fig. 5(b). A direct comparison of the radiographs acquired from the standard duplex-wire type IQI (Fig. 5(c) and 5(d)) reveals distinct differences in image texture. While the reference planar scintillator exhibits sharp edge definition, the PhC-integrated scintillator preserves comparable feature visibility. Notably, the image captured by the PhC-enhanced scintillator appears substantially smoother with reduced granularity. To quantitatively assess this effect, grayscale intensity cross-sections were extracted across representative line-pair regions (Fig. 5(f)). The PhC-based scintillator displays a notably stabilized baseline with strongly suppressed signal fluctuations relative to the reference sample, which is characterized by higher noise components. Statistical analysis performed over 14 independent regions of interest (Fig. S2 and S3) reveals that the PhC sample achieves an average SNR of (38.29 ± 0.06) dB across three independently fabricated samples, compared to only 25.3 dB for the reference sample, as detailed in Table S3. Consistent with this, the contrast-to-noise ratio (CNR) also improved from 3.04 to 4.51 (Table S4). This substantial (12.94 ± 0.06) dB improvement (corresponding to a (4.437 ± 0.033)-fold enhancement in linear SNR) supports that the enhanced photon extraction contributes effectively to improved imaging SNR. The observed SNR gain closely correlates with the (4.64 ± 0.11)-fold integrated light-output enhancement measured spectroscopically (Fig. 4(a) and Fig. S7), indicating that the extracted photon flux effectively contributes to the imaging signal rather than being redistributed as incoherent background noise.

While the SNR improvement is substantial, it is crucial to determine if this sensitivity gain comes at the cost of image sharpness. We further characterize the spatial resolution limit by imaging a slanted tungsten edge and calculating the modulation transfer function (MTF) (Fig. 5(e)). Theoretically, the introduction of a diffractive interface inevitably leads to a broader angular distribution of the outgoing wavefront, which in turn produces a modest broadening of the line spread functions (LSF) compared to the transmission of the planar reference scintillator (as detailed in Fig. S4 and Table S7). Experimentally, the limiting spatial resolution—defined at an MTF value of 0.1—decreases from 27.5 lp/mm for the reference sample to 22.8 lp/mm for the PhC sample. This moderate reduction is likely associated with the combined effects of the introduced diffractive interface and non-negligible incoherent scattering caused by structural imperfections in the self-assembled PhC layer. These effects can broaden the effective spatial response of the scintillator, as supported by the LSF broadening analysis (Table S7) and the reproducibility analysis in Fig. S8. Overall, this approximately 17% reduction reflects the trade-off associated with PhC-assisted outcoupling, including angular redistribution and possible incoherent scattering from structural imperfections, while the resolution remains sufficient for the present high-fidelity imaging demonstrations. The practical utility of this balance is visually demonstrated in the X-ray imaging of a complex integrated circuit (IC) chip (Fig. 5(g)). In this application, the PhC-enhanced scintillator delivers high-contrast radiographs where fine features—such as bonding wires with diameters of ~30 μm—remain clearly resolvable, confirming that the moderate angular broadening does not substantially compromise feature recognition capabilities. Overall, our device successfully navigates the inherent sensitivity-resolution trade-off, achieving a 13 dB SNR enhancement while maintaining a spatial resolution finer than 25 μm. This scalable diffraction-mediated extraction strategy effectively bridges the gap between high spatial resolution and sensitivity under low-light conditions, offering a compelling solution for high-performance X-ray imaging.

4 Conclusions

In summary, we demonstrate that integrating large-area photonic crystal layers via interfacial self-assembly provides a scalable strategy for enhancing the LEE of high-density inorganic scintillators. By leveraging Marangoni convection, large-area PhC monolayers with locally ordered domains are successfully fabricated. This approach reduces the reliance on sophisticated top-down nanofabrication while enabling large-area integration. The PhC-integrated scintillator realizes a 4.64-fold enhancement in integrated light output under the present collection geometry. Spectral analysis supports that this enhancement mainly originates from diffraction-assisted momentum coupling, while structural imperfections may also contribute to broadband incoherent outcoupling. Although the diffractive interface introduces a moderate trade-off in spatial resolution, the enhanced photon extraction translates into an approximately 13 dB improvement in SNR, offering an advantage for imaging under photon-starved conditions. Overall, this work provides a potentially scalable and material-compatible route toward high-sensitivity radiographic imaging, particularly in photon-starved scenarios such as low-dose medical diagnostics and rapid security screening.

References

1. Lecoq P, Gektin A, Korzhik M. *Inorganic Scintillators for Detector Systems* 2nd ed (Springer, Cham, 2017).
2. Lecoq P. Development of new scintillators for medical applications. *Nucl Instrum Methods Phys Res Sec A Accel Spectrom Detect Assoc Equip* **809**, 130–139 (2016).
3. Ma TY, Wei QY, Lyu ZL et al. Self-collimating SPECT with multi-layer interspaced mosaic detectors. *IEEE Trans Med Imaging* **40**, 2152–2169 (2021).
4. Zheng R, Chen JB, Liu YL et al. Advance in lutetium yttrium silicate scintillation crystal for all-digital PET. *CT Theory Appl* **33**, 405–420 (2024).
5. Zhou JE, An K, He P et al. Solution-processed lead-free perovskite

nanocrystal scintillators for high-resolution X-ray CT imaging. *Adv Opt Mater* **9**, 2002144 (2021).
6. Zhang TY, Dong XZ, Xu F et al. Advances and challenges in X-ray-excited scintillators and their biomedical applications: current insights and future directions. *ACS Appl Mater Interfaces* **17**, 22138–22160 (2025).
7. You FL, Lin SS, Qiao XS et al. Amorphous engineering of transparent high-crystallinity luminescent nano-glass-ceramics for advanced photonic applications. *Adv Mater* **38**, e20325 (2026).
8. Pei XQ, Zeng LW, Chen DQ. Luminescent metal-organic framework glasses: challenges in quantum dot integration and rare earth doping. *Coord Chem Rev* **557**, 217691 (2026).
9. Jin SL, Zhu SY, Wei LY et al. Near-infrared emitting lead-free perovskite scintillators for X-ray imaging with suppressed optical crosstalk. *Laser Photonics Rev* **20**, e02436 (2026).
10. Lai JA, Ye Y, Liu X et al. Triplet exciton harvesting via TADF in hafnium chlorides array scintillator screen enables ultrahigh-resolution X-ray imaging. *Opto-Electron Adv* **9**, 250273 (2026).
11. Salway H, Chua XW, Anaya M. Metal-organic frameworks as potential materials for X-ray detectors: recent progress and unique opportunities. *Mater Horiz* **12**, 8989–9008 (2025).
12. Zhu WJ, Ma WB, Su YR et al. Low-dose real-time X-ray imaging with nontoxic double perovskite scintillators. *Light Sci Appl* **9**, 112 (2020).
13. Lin ZY, Lv SC, Yang ZM et al. Structured scintillators for efficient radiation detection. *Adv Sci* **9**, 2102439 (2022).
14. Singh P, Dosovitskiy G, Bekenstein Y. Bright innovations: review of next-generation advances in scintillator engineering. *ACS Nano* **18**, 14029–14049 (2024).
15. Hou B, Chen QS, Yi LY et al. Materials innovation and electrical engineering in X-ray detection. *Nat Rev Electr Eng* **1**, 639–655 (2024).
16. Minns A, Mahajan T, Tokranov V et al. Device response principles and the impact on energy resolution of epitaxial quantum dot scintillators with monolithic photodetector integration. *Sci Rep* **14**, 22870 (2024).
17. Zhang XF, Zhu YL, Huang YS et al. Interpretable low-dose CT enhancement via multi-Gaussian cluster variance reduction. *Opto-Electron Sci* **5**, 250042 (2026).
18. Kurman Y, Shultzman A, Segal O et al. Photonic-crystal scintillators: molding the flow of light to enhance X-ray and γ-ray detection. *Phys Rev Lett* **125**, 040801 (2020).
19. Shultzman A, Segal O, Kurman Y et al. Enhanced imaging using inverse design of nanophotonic scintillators. *Adv Opt Mater* **11**, 2202318 (2023).
20. Zhu ZC, Wu S, Xue CF et al. Enhanced light extraction of scintillator using large-area photonic crystal structures fabricated by soft-X-ray interference lithography. *Appl Phys Lett* **106**, 241901 (2015).
21. Yuan D, Liu B, Guo YZ et al. Light output enhancement of scintillators by using mixed-scale microstructures. *Opt Express* **29**, 24792–24803 (2021).
22. Singh B, Marshall MSJ, Waterman S et al. Enhanced scintillation light extraction using nanoimprinted photonic crystals. *IEEE Trans Nucl Sci* **65**, 1059–1065 (2018).
23. Roques-Carmes C, Rivera N, Ghorashi A et al. A framework for scintillation in nanophotonics. *Science* **375**, eabm9293 (2022).
24. Liu FY, Yang YL, Liu YD et al. Large energy resolution improvement of LYSO scintillator by electron beam lithography method. *AIP Adv* **10**, 025101 (2020).
25. Li ZJ, Shi H, Li BN et al. Fabrication of large-area photonic crystal-modified X-ray scintillator imager for optical coding imaging. *Opt Express* **32**, 8877–8886 (2024).
26. Modrzynski P, Gotszalk T, Knapitsch A et al. Light extraction from scintillating crystals enhanced by photonic crystal structures patterned by focused ion beam. *IEEE Trans Nucl Sci* **63**, 644–648 (2016).
27. Yu HN, Meng XY, Yang SM et al. Photonic-crystals-based GAGG: Ce scintillator with high light output and fast decay time for soft X-ray detection. *Nucl Instrum Methods Phys Res Sec A Accel Spectrom Detect Assoc Equip* **1032**, 166653 (2022).
28. Liu JL, Liu B, Zhu ZC et al. Modified timing characteristic of a scintillation detection system with photonic crystal structures. *Opt Lett* **42**, 987–990 (2017).
29. Guo H, Ma JJ, Zhang FF et al. A cost-effective and scalable chemical vapor deposition method for lead-free $Cs_3Cu_2Cl_5$ scintillators with enhanced radioluminescence suitable for high-performance X-ray imaging. *Adv Opt Mater* **13**, e02322 (2025).
30. Chen XY, Liu B, Wu Q et al. Enhanced light extraction of plastic scintillator using large-area photonic crystal structures fabricated by hot embossing. *Opt Express* **26**, 11438–11446 (2018).
31. Martin-Monier L, Pajovic S, Abebe MG et al. Large-scale self-assembled nanophotonic scintillators for X-ray imaging. *Nat Commun* **16**, 5750 (2025).
32. Liu YD, Liu FY, Tang W et al. Light extraction enhancement of BGO scintillator by monolayers of SiO_2 periodic array. *AIP Adv* **9**, 105217 (2019).
33. Gannon G, Greer JC, Larsson JA et al. Molecular dynamics study of naturally occurring defects in self-assembled monolayer formation. *ACS Nano* **4**, 921–932 (2010).
34. Zhu ZC, Liu B, Zhang F et al. Improved light output from thick β-Ga_2O_3 scintillation crystals via graded-refractive-index photonic crystals. *Opt Express* **29**, 18646–18653 (2021).
35. Mino L, Borfecchia E, Segura-Ruiz J et al. Materials characterization by synchrotron X-ray microprobes and nanoprobes. *Rev Mod Phys* **90**, 025007 (2018).
36. Xu XW, Xie YM, Shi HY et al. Light management of metal halide scintillators for high-resolution X-ray imaging. *Adv Mater* **36**, 2303738 (2024).
37. Zhong Y, Yu XJ, Li WW. Nanoscale scintillating materials for X-ray imaging: fundamentals and applications. *J Mater Chem C* **13**, 1036–1062 (2025).
38. Cai YJ, Zhang BM. Marangoni flow-induced self-assembly of hexagonal and stripelike nanoparticle patterns. *J Am Chem Soc* **130**, 6076–6077 (2008).
39. Lin X, Fang GQ, Liu YL et al. Marangoni effect-driven transfer and compression at three-phase interfaces for highly reproducible nanoparticle monolayers. *J Phys Chem Lett* **11**, 3573–3581 (2020).
40. Nikl M, Yoshikawa A. Recent R&D trends in inorganic single-crystal scintillator materials for radiation detection. *Adv Opt Mater* **3**, 463–481 (2015).
41. Zhu Y, Qian S, Wang ZG et al. Scintillation properties of GAGG: Ce ceramic and single crystal. *Opt Mater* **105**, 109964 (2020).
42. Dimitrakopoulos A, Michail C, Valais I et al. Experimental evaluation of GAGG: Ce crystalline scintillator properties under X-ray radiation. *Crystals* **15**, 590 (2025).
43. Schreiber F. Structure and growth of self-assembling monolayers. *Prog Surf Sci* **65**, 151–257 (2000).
44. Liu TY, Solomon MJ. Reconfigurable grating diffraction structural color in self-assembled colloidal crystals. *Small* **19**, 2301871 (2023).
45. Lee SG, Kim SH, Lee WJ. Merging and band transition of bound states in the continuum in leaky-mode photonic lattices. *Laser Photonics Rev* **17**, 2300550 (2023).
46. Hong KS, Lim HJ, Ko YH et al. Boosting single-photon extraction efficiency in GaN through radiative mode conversion. *Laser Photonics Rev* **19**, 2401966 (2025).
47. Tan ATL, Nagelberg S, Chang-Davidson E et al. In-plane direct-

write assembly of iridescent colloidal crystals. *Small* **16**, 1905519 (2020).
48. Zhu Z, Liu B, Cheng C et al. Broadband light output enhancement for scintillator using whispering-gallery modes in nanospheres. *Physica Status Solidi (A)* **211**, 1583–1588 (2014).
49. Zhu ZC, Liu B, Cheng CW et al. Improved light extraction of LYSO scintillator by the photonic structure from a layer of anodized aluminum oxide. *Nucl Instrum Methods Phys Res Sec A Accel Spectrom Detect Assoc Equip* **786**, 1–4 (2015).
50. Ouyang X, Liu B, Xiang XC et al. Enhanced light output of CsI (Na) scintillators by photonic crystals. *Nucl Instrum Methods Phys Res Sec A Accel Spectrom Detect Assoc Equip* **969**, 164007 (2020).
51. Yuan D, Liu B, Zhu ZC et al. Directional control and enhancement of light output of scintillators by using microlens arrays. *ACS Appl Mater Interfaces* **12**, 29473–29480 (2020).
52. Strassberg R, Nakanishi A, Shamaev B et al. Self-assembled colloidal photonic structures for directional radioluminescence of Gd and Ta oxide scintillators. *Adv Opt Mater* **12**, 2401030 (2024).

Acknowledgements

We are grateful for financial support from the Natural Science Foundation of Chongqing, China under grant CSTB2025NSCQ-LZX0041, the Development Foundation of 26th Institute of China Electronics Technology Group Corporation under grant K2605ZZ2025002, the Beijing Natural Science Foundation under Grant L242114 and the National Key Research and Development Program of China under Grant 2019YFC0605203.

Author contributions

The manuscript was written through contributions of all authors. Y. Zhu performed the main experiments and measurements, and conducted simulations. C. Li analyzed the results and edited the manuscript. S. Cao and J. Lai contributed to the experiments and figure refinement. P. He helped to conduct X-ray imaging. K. Liu, P. Feng and Y. Ding conceived the original idea and supervised the project. Q. Wang and X. Xiao coordinated the project administration and provided research resources. All authors have reviewed and approved the final manuscript.

Competing interests

The authors declare no competing financial interests.

Supplementary information

Supplementary information for this paper is available at
https://doi.org/10.29026/oea.2026.260038